

Trimetallic Pentlandites (Fe,Co,Ni)₉S₈ for the Electrocatalytical HER in Acidic Media

Mathias Smialkowski, Daniel Siegmund, Kenta Stier, Lars Hensgen, Marek P. Checinski,* and Ulf-Peter Apfel*



Cite This: *ACS Mater. Au* 2022, 2, 474–481



Read Online

ACCESS |

Metrics & More

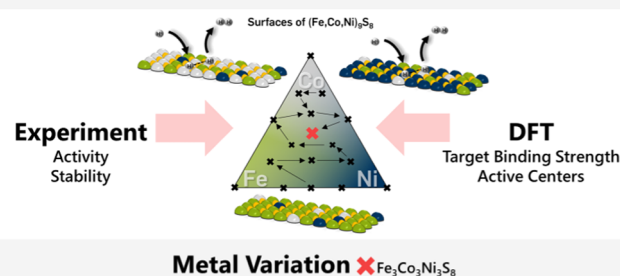
Article Recommendations

Supporting Information

ABSTRACT: Recently, pentlandite materials have been shown to exhibit promising properties with respect to the hydrogen evolution reaction (HER). A whole series of trimetallic FeCoNi-pentlandite materials and composites have been synthesized from the elements using high-temperature synthesis and categorized in terms of purity. Furthermore, the electrocatalytic properties regarding the HER were determined and correlated to hydrogen adsorption energies, which were determined by means of density functional theory (DFT) calculations. The relationships between activity and its origin generated in this way help to better understand the pentlandite system and provide meaningful approaches for catalyst synthesis.

KEYWORDS: HER, hydrogen evolution reaction, pentlandite, trimetallic pentlandite, sulfide materials, catalyst poison, DFT

TRIMETALLIC PENTLANDITE-BASED HER CATALYSTS



INTRODUCTION

Establishing a green hydrogen-based economy is one of the major challenges of the current century to mitigate climate change. Herein, electrolyzers are an elegant way to produce green hydrogen with electrical energy from fluctuating renewables. However, a variety of obstacles must be overcome to master this venture. Among them is the use of efficient electrocatalysts for the hydrogen evolution reaction (HER) under acidic conditions, which should offer a high activity and stability.¹ Further, the catalyst should be cheap and environmentally benign.² Currently, precious platinum is the only industrially used material for this purpose but is of limited availability. Recently, metal-rich transition-metal chalcogenides emerged as promising alternatives for traditional precious-metal-based hydrogen evolution catalysts. In particular, pentlandite materials (Pn) of the general formula M₉X₈, where M is a transition metal and X is a chalcogenide, have been proven to be potent candidates to replace platinum due to their high HER activity and durability also in the presence of common catalyst poisons such as H₂S and CO.^{3,4} The elemental composition of pentlandites is very flexible and a targeted synthesis of Pn materials with precise stoichiometric control can be achieved by various routes, including hydrothermal, mechanochemical, and solid-state methods.^{4–9} Along this line, alteration of catalyst composition allowed for a preliminary optimization of the catalyst HER activity and (Fe,Ni)₉S₈, (Fe,Co)₉S₈, (Ni,Co)₉S₈, and (Fe,Ni)₉S_{8–x}Se_x (x = 1–8) were shown to be suitable lead structures.^{10–13} To find more effective catalysts, we recently synthesized trimetallic

pentlandites (Fe,Co,Ni)₉S₈ with different metal ratios, leading to an application patent for acidic HER.¹⁴ While syntheses and applications were subsequently reported in detail, important activity–structure correlations for HER of this class of materials have been discussed only succinctly.^{15,16} In this study, we probe the accessibility of conceivable trimetallic pentlandite phases and provide a hitherto unparalleled analysis of their catalytic activity in HER in conjunction with density functional theory (DFT) calculations. Thus, we derive conclusive insights into the structure/activity relationship of this catalyst class.

MATERIAL SYNTHESIS AND CHARACTERIZATION

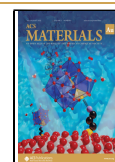
The trimetallic pentlandites Fe₃Co_{6–x}Ni_xS₈, (x = 1–5), Fe_{6–x}Co₃Ni_xS₈, (x = 1–5), Fe_{6–x}Co_xNi₃S₈ (x = 1–5) as well as FeCoNi₇S, Fe₇CoNi₈ and Fe_{1.6}Co_{5.6}Ni_{1.8}S₈, were synthesized following our previously established high-temperature route from the elements.^{10–12,17} The exact experimental conditions and adjustments are provided in the Supporting Information (Table S1). Subsequently, the materials were characterized via differential scanning calorimetry (DSC) and

Received: February 8, 2022

Revised: April 8, 2022

Accepted: April 8, 2022

Published: April 27, 2022



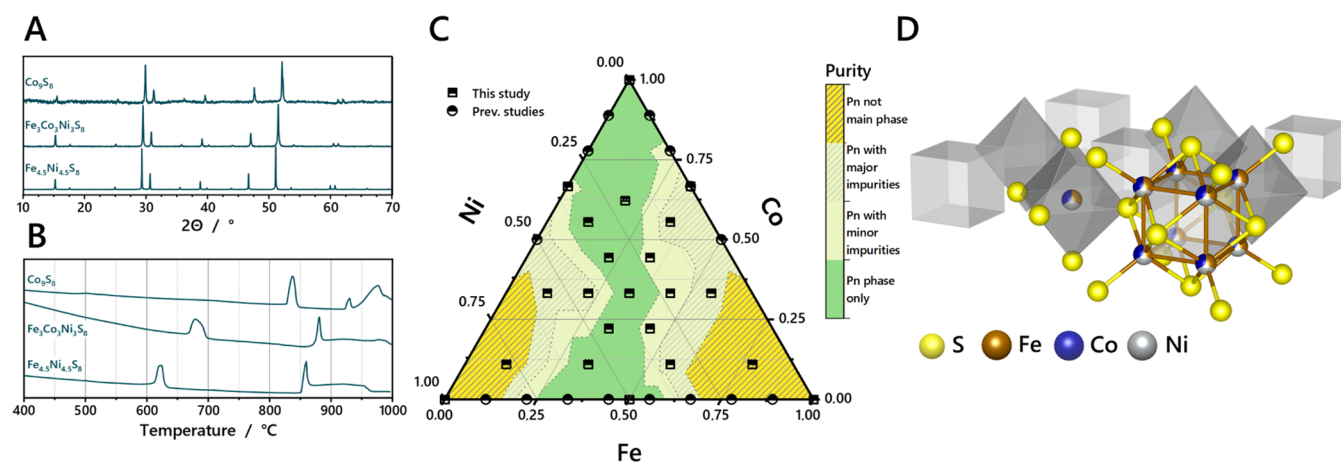


Figure 1. Powder diffraction pattern (A) and thermal analysis via DSC (B) of Co_9S_8 , $\text{Fe}_{4.5}\text{Ni}_{4.5}\text{S}_8$, and $\text{Fe}_3\text{Co}_3\text{Ni}_3\text{S}_8$. Ternary plot (C) shows Fe–Co–Ni sulfide system including various M_9S_8 -type materials from this and previous studies and gives relation to phase-purity via colorized topology map.^{10,12} Crystal structure (D) represents the $\text{Fe}_3\text{Co}_3\text{Ni}_3\text{S}_8$ pentlandite structure.

powder X-ray diffraction (PXRD) to confirm the characteristic phase transitions as well as the phase composition. Exemplary DSC and PXRD data of the Co_9S_8 , $\text{Fe}_{4.5}\text{Ni}_{4.5}\text{S}_8$, and $\text{Fe}_3\text{Co}_3\text{Ni}_3\text{S}_8$ are shown in Figure 1A,B. In DSC, most compounds show the characteristic pentlandite phase transitions between 600–700 and 800–900 $^\circ\text{C}$, previously described by Sugaki et al., confirming typical Pn-type behavior (Figures S1–S3).⁹

However, DSC and PXRD also revealed the monometallic Fe_9S_8 and Ni_9S_8 to be mixtures of various iron sulfides or nickel sulfides (Figure S4), respectively, while Co_9S_8 is the only phase-pure monometallic pentlandite (Figure 1C). This was to be expected, as the pentlandite phase has been shown to be unstable at very high Fe or Ni contents.^{10,18} In analogy, the bimetallic compounds were synthesized according to previous procedures, by either mechanochemical or high-temperature pathways and exhibit the previously reported PXRD features (Figure S5).^{4,12} Notably, the trimetallic pentlandite phase is present within very wide limits in the ternary Fe–Co–Ni sulfide system (Figure 1C). These limits are defined by the fact that a high cobalt content leads to rising amounts of impurities (pyrrhotite-like TMS) at a fixed iron content ($\text{Fe}_3\text{Co}_{6-x}\text{Ni}_x\text{S}_8$, Figure S6A). Furthermore, for compounds with a fixed nickel content ($\text{Fe}_{6-x}\text{Co}_x\text{Ni}_3\text{S}_8$, Figure S6C), a rather high content of iron turns out to cause increasing amounts of additional phases, i.e., corresponding nonpentlandite binary metal sulfides, like FeS and NiS. Along this line, compounds with fixed cobalt content, both, with high Fe and high Ni content show equally increasing amounts of extra phases ($\text{Fe}_x\text{Co}_3\text{Ni}_{6-x}\text{S}_8$, Figure S6B), due to previously explained limitations by Fe or Ni (Figure 1C).^{10,18} However, these borders are even narrower for trimetallic compounds with three cobalt equivalents, where only Fe/Ni ratios close to 1:1 result in completely phase-pure materials. Despite the observed impurities, the pentlandite phase constitutes the main phase in the majority of trimetallic compounds or can be identified as at least a secondary phase. Furthermore, while cobalt-rich compounds are mainly phase-pure, the iron-rich as well as nickel-rich compounds only contained the pentlandite phase next to several other sulfidic phases (Figures S4–S7) and thus must be considered as composites rather than single-phase materials. This especially becomes important when dealing

with their electrochemical behavior, as these can have quite complex and intricate properties.^{19–21}

The overall elemental composition of the compounds was additionally investigated via SEM-EDX (Figures S8–S10) and reveals a uniform element distribution within phase-pure pentlandite materials exposing only randomly fractured particles with no defined morphologies with a broad particle size distribution. To further confirm the nature of the compounds, Co_9S_8 , $\text{Fe}_{4.5}\text{Ni}_{4.5}\text{S}_8$, and $\text{Fe}_3\text{Co}_3\text{Ni}_3\text{S}_8$ were exemplarily investigated via X-ray photoelectron spectroscopy. The spectra show the expected signals in their typical energy regions concomitant with a surficial oxidation even after Ar^+ sputtering (Figures S12–S14).

To gain insight into the material structure, crystals were grown for the trimetallic pentlandite $\text{Fe}_3\text{Co}_3\text{Ni}_3\text{S}_8$ via vapor-transport methods.⁹ The structure (Figure 1D) was determined by single-crystal X-ray diffraction methods (XRD) and is compared with previously obtained structures for the monometallic pentlandite Co_9S_8 and bimetallic $\text{Fe}_{4.5}\text{Ni}_{4.5}\text{S}_8$.^{11,22–24} The selection allows for complementary insight into the elemental positions and bonding situation within the crystals (Table S2). The data match the previously obtained crystal information from PXRD. The materials form isomorphic structures in the same cubic space group $Fm\bar{3}m$ —as expected for a pentlandite phase. Interestingly, the cell constant significantly shortens with the introduction and increasing amounts of cobalt from $\text{Fe}_{4.5}\text{Ni}_{4.5}\text{S}_8$ over $\text{Fe}_3\text{Co}_3\text{Ni}_3\text{S}_8$ to Co_9S_8 . Accordingly, the mean bond lengths change to overall shorter distances, with an exception at the octahedral metal site, where the mean bond length is shortest for $\text{Fe}_3\text{Co}_3\text{Ni}_3\text{S}_8$ with 2.376 Å, but longest for Co_9S_8 with 2.482 Å, while $\text{Fe}_{4.5}\text{Ni}_{4.5}\text{S}_8$ has 2.421 Å (Table S3). This behavior points to a certain preferential occupation of the available atom sites by the different metal, e.g., preferential occupation of Fe at the octahedral metal site.²⁵ Similar observations were made for the tetrahedral coordinated metal in the cluster. Here, the $\text{M}_t\text{—S}$ bond length slightly decreases from 2.166 Å after the introduction of cobalt to 2.146 Å and slightly increases to 2.149 Å for Co only. As a result, the metal center distances near the position Wyckoff 8C—the previously determined “sulfur depletion site”, which is attributed a key role in the formation of an HER-active Pn-surface—is slightly shortened for the $\text{Fe}_3\text{Co}_3\text{Ni}_3\text{S}_8$ (3.505 Å) compared to the Co_9S_8 (3.510

Table 1. Key Values η_{50} , as well as Tafel Slopes, Exchange Current Densities $\log(j_0)$, and C_{DL} Taken from Data at 25 °C (and 75 °C)^a

| compound | η_{50} "pre", mV _{RHE} | η_{50} "post", mV _{RHE} | Tafel "pre", mV dec ⁻¹ | Tafel "post", mV dec ⁻¹ | C_{DL} "pre", μ F | C_{DL} "post", μ F |
|--|--------------------------------------|---------------------------------------|-----------------------------------|------------------------------------|-------------------------|--------------------------|
| Co ₉ S ₈ | 364 (302) | 425 (322) | 148 (145) | 139 (125) | 67.4 (63.9) | 48.1 (59.3) |
| Ni ₃ Co ₆ S ₈ * | 405 | 373 | 118 | 88 | 16.6 | 12.9 |
| Fe _{4.5} Ni _{4.5} S ₈ | 385 | 379 | 78 | 86 | 10.1 | 20.1 |
| Fe ₃ Co ₃ Ni ₃ S ₈ | 376 (298) | 385 (297) | 114 (88) | 100 (101) | 22.1 (42.1) | 28.5 (24.2) |
| Fe ₃ Co ₂ Ni ₄ S ₈ | 394 | 388 | 102 | 94 | 6.9 | 8.8 |
| Fe ₃ CoNi ₅ S ₈ | 383 | 365 | 92 | 85 | 12.0 | 14.6 |
| Fe ₄ Co ₃ Ni ₂ S ₈ * | 412 | 388 | 111 | 97 | 47.3 | 52.3 |
| FeCo ₅ Ni ₃ S ₈ | 406 | 387 | 113 | 96 | 9.3 | 11.6 |
| Fe ₂ Co ₄ Ni ₃ S ₈ | 378 | 390 | 108 | 109 | 35.8 | 33.9 |
| Fe _{1.6} Co _{5.6} Ni _{1.8} S ₈ | 399 | 394 | 108 | 84 | 16.3 | 18.6 |

^aThe values "pre" or "post" 2 h electrolysis at -300 mA cm⁻² are listed; "*" marks composite compounds.

Å) and Fe_{4.5}Ni_{4.5}S₈ (3.537 Å) (Figure S15).^{3,22} Assuming a similar potential for reductive depletion of sulfur for all pentlandite systems, changes to this position may also result in altered activities for the HER.^{11,13}

■ ELECTROCATALYTIC HYDROGEN EVOLUTION

Electrochemical analysis of material pellets was performed in an H-type cell utilizing sulfuric acid as an electrolyte at 25 and 75 °C. In this setup, the cathode and anode were separated by a membrane to avoid cross-contamination of the electrodes by ion-redeposition, which was further excluded by postmortem analysis (Figure S11). The values are listed in Table 1 for selected representatives and in Tables S4–S6 for all compounds made within this study. Tafel analysis yields valuable information about the respective kinetic limitations due to different M–H binding modes and involved catalytic centers (Figures S16 and S17).^{3,26} A Volmer–Heyrovsky-based mechanism is expected for very high Tafel slopes, like 148 mV dec⁻¹ for Co₉S₈ and 114 mV dec⁻¹ for Fe₃Co₃Ni₃S₈, including the chemisorption of a solvated proton with a subsequent reaction of this species with another solvated proton. In contrast, Fe_{4.5}Ni_{4.5}S₈ shows a rather low Tafel slope of 78 mV dec⁻¹, which is assigned to a Volmer–Tafel-type reaction, where the fast chemisorption of protons to the surface is followed by a rate-limiting recombination reaction directly on the catalyst surface. This mechanism also applies for platinum electrode references with a Tafel slope of 46 mV dec⁻¹. Regarding pentlandites, the Tafel slope increases with increasing Co content, while compounds containing Fe or Ni usually exhibit significantly lower values. Thus, a Volmer–Heyrovsky-based mechanism is assumed for Co-rich trimetallic materials (Table S4) and the reaction mechanism shifts to a Volmer–Tafel-type pathway with increasing Fe or Ni content.

To probe the electrochemical HER behavior, we evaluated and compared the overpotentials η_{50} at -50 mA cm⁻² (Figure 2A). The values are within a range of 320–490 mV_{RHE} at 25 °C (Table S5). The values show the interesting progression from high to low iron contents that the HER performance decreases noticeably, with a Ni-only sulfide composite "Ni₉S₈" being the most active material, while an iron-exclusive sulfide composite "Fe₉S₈" exhibits the lowest activity. Considering the complex phase composition of the materials, the different reactivities might be attributed to phase-dependent interplays or display decomposition processes. A focused look on the phase-pure compounds, however, reveals that the overpotential decreases when going from high iron or nickel content to a more balanced Fe/Ni distribution (Figure 2B).

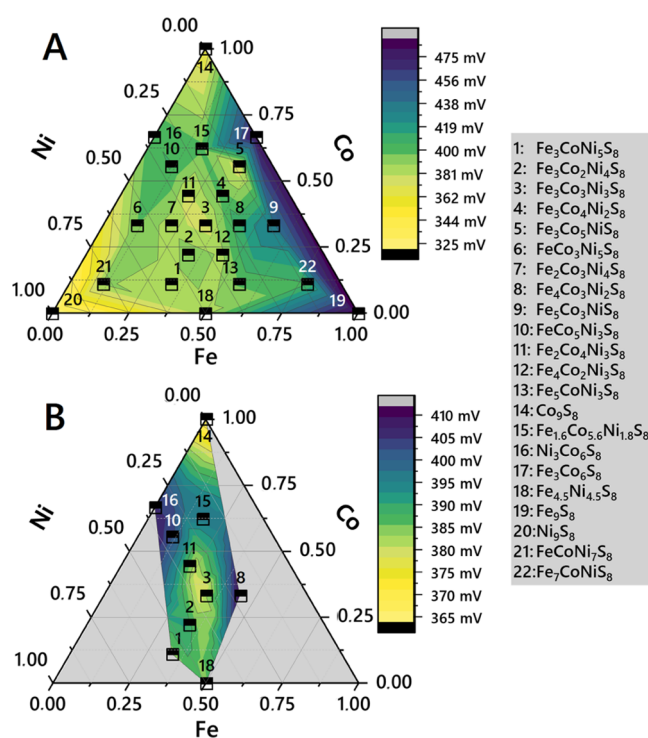


Figure 2. Ternary plots of the Fe–Co–Ni sulfide system. The topology maps give the initial η_{50} values from LSV (Figure S18) at 25 °C. (A) All materials and composites of the study and (B) only a selection of almost phase-pure compounds.

Furthermore, following the trajectory, higher cobalt contents are preferable to achieve an initially increased HER activity as well. Here, it is noticeable that there is a clear benefit from the incorporation of close to or equal amounts of elements, having Fe₃Co₃Ni₃S₈ in the center (376 mV_{RHE}). Likewise, the high Co share in Co₉S₈ is beneficial as the pure, as-synthesized substance reveals the initially highest activity (364 mV_{RHE}). It is remarkable that upon metal variation, which causes only subtle changes in the materials electronics, the HER activity, as well as the respective reaction mechanism, as shown by Tafel analysis, can be varied with no elaborate surface structuring as needed for other metal chalcogenide catalysts.^{27–29} Thus, to allow for judgment on the variation of active sites due to metal exchange, the electrochemically active surface area (ECSA) was determined (Table S6).^{3,11,17} In theory, the higher the ECSA—usually represented by the double-layer capacity C_{DL} —the more active sites are available for the HER. The

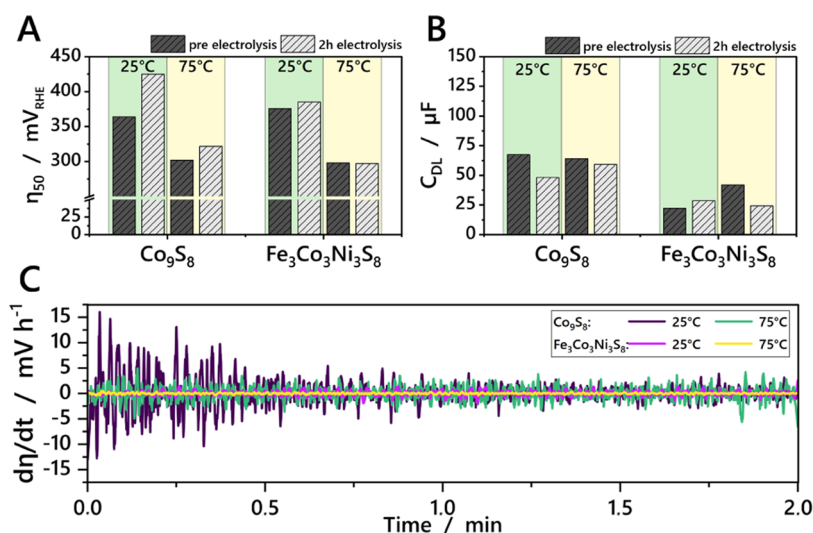


Figure 3. (A) Overpotentials before and after 2 h of electrolysis at -300 mA cm^{-2} and either 25 or 75 °C, respectively, for Co_9S_8 and $\text{Fe}_3\text{Co}_3\text{Ni}_3\text{S}_8$ obtained from LSVs at -50 mA cm^{-2} . (B) Electrochemically active surface area (ECSA) represented by the double-layer capacitance (C_{DL}) obtained from CVs before and after 2 h electrolysis at -300 mA cm^{-2} at 25 and 75 °C. (C) First derivative of overpotential curves obtained after 2 h electrolysis at -300 mA cm^{-2} .

cobalt pentlandite Co_9S_8 shows the highest C_{DL} at 25 °C with $67.40 \mu\text{F}$, followed by “ Ni_9S_8 ” ($23.54 \mu\text{F}$), $\text{Fe}_3\text{Co}_3\text{Ni}_3\text{S}_8$ ($22.13 \mu\text{F}$), $\text{Ni}_3\text{Co}_6\text{S}_8$ ($16.58 \mu\text{F}$), $\text{Fe}_{4.5}\text{Ni}_{4.5}\text{S}_8$ ($10.11 \mu\text{F}$), and $\text{Fe}_3\text{Co}_6\text{S}_8$ ($5.88 \mu\text{F}$) with the other compounds showing intermediate values (Figures S20–S25). The activity trend derived from the overpotentials is thus reflected in these measurements. However, a notable exception is the Fe-rich composite “ Fe_9S_8 ”, which has a very high C_{DL} of $56.24 \mu\text{F}$, albeit showing low activity. This again underlines that material alteration and various ad- and desorption processes have a great impact on the activity as well and explain variations observed for other composites measured. An isolated look reveals the phase-pure compounds Co_9S_8 and $\text{Fe}_3\text{Co}_3\text{Ni}_3\text{S}_8$ to follow this trend (Figure 3B) as well.

While the described trend would obviously favor Co_9S_8 as a better catalyst, for an application, this performance must be kept for an extended period of time with low decay rates at elevated current densities.¹ Notably, the trend is well preserved for η_{10} (Figures S18 and S19) but changes already after a short electrolysis. To fully investigate the catalyst performance, stability measurements are thus key. Therefore, the stability of the materials was subsequently investigated via chronopotentiometry at -300 mA cm^{-2} for a period of 2 h (Figures S26 and S27) at 25 and 75 °C (Table S5). Different activation and deactivation behaviors can be observed for the materials. Obviously, while being most active in terms of initial LSV measurements, Co_9S_8 shows a significant deactivation, raising its η_{50} by over 60 mV (25 °C) and 20 mV (75 °C) as seen in Figure 3A. The evaluation of C_{DL} reveals tolerable changes in the ECSA after long-time experiments (Figure 3B). Moreover, the first derivative of the Co_9S_8 chronopotentiometry curve perfectly highlights the large changes in the overpotential with time, stressing the low stability of the as-synthesized material during electrolysis (Figure 3C). In contrast, the potential is virtually constant for $\text{Fe}_3\text{Co}_3\text{Ni}_3\text{S}_8$ at 25 °C as well as 75 °C, representing a significantly higher degree of stability and rendering it a preferable catalyst material than pure Co_9S_8 . Extended stability measurements of $\text{Fe}_3\text{Co}_3\text{Ni}_3\text{S}_8$ for 72 h at -300 mA cm^{-2} also show good stability of the material (Figure S28). The test implementation of the catalyst in a PEM cell

also showed good stability over the experimental period of 10 h (Figure S33).

The materials seemingly undergo a mixed thermal/electrochemical altering process under reductive conditions depending on phase composition and purity. For $(\text{Fe},\text{Ni})_9\text{S}_8$ type pentlandites, this behavior can partially be attributed to sulfur depletion reactions, a process generally involved for Pn-type materials.²² However, this effect seems less important for Co-rich materials indicated by a largely stable ECSA under reductive conditions as well as SEM-EDX postmortem analysis (Figure S11), thereby suggesting a stronger Co–S interaction in these materials, as shown by the smaller bond length at the depletion sites. It is therefore likely that additional processes, especially in composite materials as well as materials with highly heterogenic Co-containing composition take place, especially in view of the pronounced deactivation behavior of Co_9S_8 while the ECSA was only moderately affected.

■ HYDROGEN ADSORPTION ENERGIES

To better assess the described findings on the activity of the various compounds and to understand their origins, the hydrogen adsorption energy ΔE_H was calculated for selected compounds. The selection was primarily limited to a few materials that best cover the different ranges of pentlandite-type compositions, namely, the monometallic Co_9S_8 ; the bimetallic compounds $\text{Fe}_{4.5}\text{Ni}_{4.5}\text{S}_8$, $\text{Ni}_{4.5}\text{Co}_{4.5}\text{S}_8$, $\text{Ni}_3\text{Co}_6\text{S}_8$, and $\text{Fe}_3\text{Co}_6\text{S}_8$; and the trimetallic $\text{Fe}_{1.6}\text{Co}_{5.6}\text{Ni}_{1.8}\text{S}_8$, $\text{Fe}_3\text{CoNi}_3\text{S}_8$, $\text{Fe}_4\text{Co}_3\text{Ni}_2\text{S}_8$, and $\text{Fe}_3\text{Co}_3\text{Ni}_3\text{S}_8$. Even though some of them were composites, the selection ensured a consistent series in the calculation of ΔE_H . The binding energies were calculated via density functional theory (DFT) as a possible descriptor for the catalyst performance during electrochemical hydrogen evolution reaction to facilitate the prediction of novel promising catalyst compositions among pentlandite materials. For this, M_9S_8 -[111]-surfaces with exposed metal sites (thus effectively emulating sulfur depletion sites) have been generated computationally and hydrogen atoms were offered (Figure S29). Examples are shown in Figure 4 for $\text{Fe}_3\text{Co}_3\text{Ni}_3\text{S}_8$ and $\text{Fe}_{4.5}\text{Ni}_{4.5}\text{S}_8$. According to Sabatier’s principle, a reactant

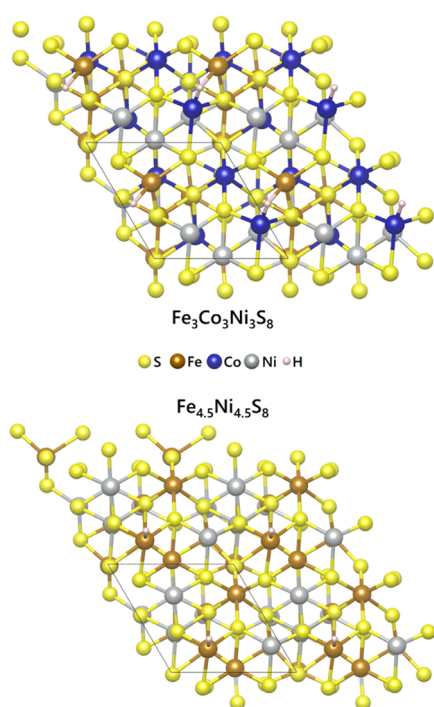


Figure 4. $2 \times 2 \times 1$ Supercell of pentlandite surfaces with adsorbed hydrogen atoms. $\text{Fe}_3\text{Co}_3\text{Ni}_3\text{S}_8$ comprises μ_2 -H, while at the $\text{Fe}_{4.5}\text{Ni}_{4.5}\text{S}_8$ surface, the H is terminally bound. Rhombus marks DFT-calculated unit cell.

should neither bind too strong nor too weak to a catalyst surface, to reach optimal performance.^{30,31} This was the basis for Nørskov et al. to develop a volcano relationship for HER catalysts, using the common logarithm of the exchange current density j_0 as a function of the hydrogen adsorption energy ΔE_{H} .³² $\log(j_0)$ is considered to give the rate of hydrogen evolution per surface area at a certain potential where the reaction is at equilibrium.

They estimated the “top” of the volcano at around -0.24 eV, which has been demonstrated and confirmed by the fact that the potent noble-metal catalysts, e.g., Pd and Pt, were approximately located in that region.

For the herein described catalysts, the adsorption energies are summarized in Table 2. Despite the fact that the calculated surfaces are merely a simplification of the real surfaces (not accounting for different phases, facets, or electrochemical alterations of the surface), initial trends in activity are expected

Table 2. H-Adsorption Energies of Different [111]-Pentlandite Surfaces Calculated via DFT^a

| surface | calc. binding mode | ΔE_{H} , eV | $\log(j_0)$, A cm^{-2} | involved metal centers |
|---|--------------------|----------------------------|----------------------------------|------------------------|
| $\text{Ni}_{4.5}\text{Co}_{4.5}\text{S}_8^*$ | μ_1 | +0.05 | -5.61 | Co |
| $\text{Ni}_3\text{Co}_6\text{S}_8^*$ | μ_1 | +0.04 | -3.27 | Co |
| $\text{Fe}_3\text{CoNi}_3\text{S}_8$ | μ_1 | -0.12 | -5.45 | Fe |
| $\text{Fe}_{4.5}\text{Ni}_{4.5}\text{S}_8$ | μ_1 | -0.14 | -6.09 | Fe |
| Co_9S_8 | μ_2 | -0.23 | -4.15 | Co Co |
| $\text{Fe}_3\text{Co}_3\text{Ni}_3\text{S}_8$ | μ_2 | -0.30 | -4.67 | Fe Co |
| $\text{Fe}_{1.6}\text{Co}_{5.6}\text{Ni}_{1.8}\text{S}_8$ | μ_2 | -0.31 | -5.01 | Fe Co |
| $\text{Fe}_4\text{Co}_3\text{Ni}_2\text{S}_8^*$ | μ_2 | -0.68 | -5.08 | Co Co |
| $\text{Fe}_3\text{Co}_6\text{S}_8^*$ | μ_2 | -0.77 | -3.90 | Fe Co |

^a“*” marks composite compounds.

to be derived.³³ To account for local differences in metal composition at H-adsorption sites, the possible permutations at each position were included in the calculations. As a first observation, it is important to note that the calculations suggest different initial H-binding modes, caused by compositional alterations, which may even change the overall mechanism of action. In general, terminal μ_1 -adsorption modes appear less favorable compared to bridging μ_2 -binding modes leading to overall more positive values of ΔE_{H} , which is expected due to a more stable hydride bonding to two metal sites in μ_2 -H bonds.

It is evident from the results that an optimal H-binding to the surface can only be achieved through the interplay of adjacent metal atoms. It is striking that the substitution of Co in Co_9S_8 for Ni to obtain $\text{Ni}_3\text{Co}_6\text{S}_8$ leads to an increase in ΔE_{H} while the additional incorporation of Fe (e.g., $\text{Fe}_3\text{Co}_6\text{S}_8$) further decreases ΔE_{H} . Thus, it appears that either Co-rich or mixed Co-Fe sites are necessary to ensure surface binding in a favorable μ_2 mode. However, the presence of Ni likewise seems to modulate the H-adsorption energy even in predominate μ_2 -binding materials as evidenced, e.g., by $\text{Fe}_3\text{Ni}_3\text{Co}_3\text{S}_8$. To shed even more light onto the observations, the metal centers involved in the preferred binding mode need to be examined. It can be observed that μ_1 -H bonds with Co in principle display higher values for ΔE_{H} compared to hydride bonds to Fe. This is only partly the case for μ_2 -H bonds as Co_9S_8 and $\text{Fe}_4\text{Co}_3\text{Ni}_2\text{S}_8$ show. Bonds involving homometallic CoCo centers are not necessarily higher in energy than mixed FeCo centers, which highlights the complexity of metal compositions. It is striking that direct bonds to surface nickel are not favored in any way, although it strongly influences the binding properties. The presence of nickel alone ensures that the adsorption energy is raised, e.g., revealed by a comparison of $\text{Fe}_3\text{Co}_6\text{S}_8$ and $\text{Fe}_3\text{Co}_3\text{Ni}_3\text{S}_8$. In numbers, Co_9S_8 is rather close to the described ideal hydrogen adsorption energy of -0.24 V, with -0.23 eV, while the deviation becomes larger for $\text{Fe}_3\text{Co}_3\text{Ni}_3\text{S}_8$ (-0.30 eV)—which is closer to the calculated value of metallic Pt (-0.27 eV)—and $\text{Fe}_{4.5}\text{Ni}_{4.5}\text{S}_8$ (-0.14 eV), while $\text{Fe}_3\text{Co}_6\text{S}_8$ marks the end with (-0.77 eV). This fits very well with the activity results from the electrochemical measurements.

CROSS-LINKING CALCULATIONS AND EXPERIMENTS

Upon comparison of these theoretical considerations to actual electrochemical measurements of $\log(j_0)$, it becomes obvious that the activity trend in an isolated view is preserved for at least Co_9S_8 , $\text{Fe}_{4.5}\text{Ni}_{4.5}\text{S}_8$ and $\text{Fe}_3\text{Co}_3\text{Ni}_3\text{S}_8$ (Figure 5). The cobalt pentlandite exhibits the highest value for the log exchange current density ($\log(j_0) = -4.15$ A cm^{-2}), followed by the trimetallic $\text{Fe}_3\text{Co}_3\text{Ni}_3\text{S}_8$ pentlandite (-4.67 A cm^{-2}) and $\text{Fe}_{4.5}\text{Ni}_{4.5}\text{S}_8$ (-6.09 A cm^{-2}), as already assumed from the adsorption energies (Table 2). Setting the calculated ΔE_{H} values for all other compounds in relation to the exchange current density $\log(j_0)$, possible activity trends may still be derived. However, while the trend is still visible, it is less pronounced in our case. Even though the calculated hydrogen adsorption energy is rather close to the value of platinum metal (-0.27 eV) for Co_9S_8 and $\text{Fe}_3\text{Co}_3\text{Ni}_3\text{S}_8$, the exchange current densities of these catalysts are considerably lower than for PGMs. In contrast, $\text{Fe}_3\text{Co}_6\text{S}_8$ and $\text{Ni}_3\text{Co}_6\text{S}_8$ show $\log(j_0)$ of -3.90 and -3.27 A cm^{-2} , although their hydrogen adsorption energies of -0.77 and 0.04 eV are relatively far from the ideal

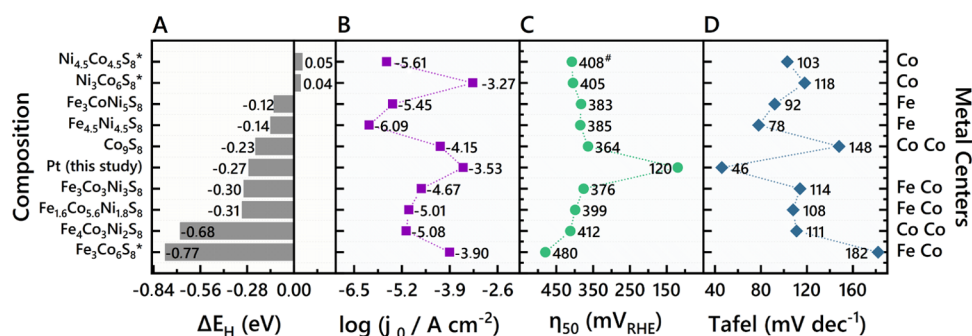


Figure 5. Graph showing (A) hydrogen adsorption energy ΔE_H , (B) common logarithm of exchange current density $\log(j_0)$, (C) overpotential η_{50} at 25 °C (# = value read at -47 mA cm^{-2}), and (D) Tafel slope of different compounds. The left Y-axis shows compound composition estimation, while the right Y-axis gives the hydrogen coordinating metal centers, both according to DFT. One metal corresponds to a terminally bound hydride, while for two metals, a bridging hydride exists; “*” marks composite materials.

value. To exclude errors in the experimental methodology, a platinum pellet electrode was measured for comparison. The values of the platinum electrode correspond to those described in the literature.^{34,35}

This leads to the conclusion that the correlation of $\log(j_0)$ and ΔE_H is best suited for bare metal electrodes but likely underestimates the complex surface compositions of our sulfidic and pelletized (composite-) materials, with a large number of conceivable active sites. Moreover, the correlation of $\log(j_0)$ and ΔE_H on its own is not sufficient as a descriptor for HER performance but needs additional considerations, like the respective η , as well as exemplarily determination of faradaic resistances to provide a clearer picture of the origin of catalysts activity. For this, the novel compounds were examined in detail for their HER capabilities, as discussed before. Displaying η_{50} compared to ΔE_H (Figure 5) yields a first hint toward a certain correlation between the adsorption of hydrogen on a catalyst surface and its electrochemical HER performance.

The overpotentials tend to decrease for compounds where ΔE_H approaches the value -0.24 eV regardless of which metal centers and binding modes are involved, confirming the expected behavior. This trend also shows up during additionally performed galvanostatic electrochemical impedance spectroscopy (gEIS) at -300 mA cm^{-2} for some selected single-phase compounds (Figures S30–S32). The data show a charge-transfer resistance (R_{CT}) of 4.802Ω for Co_9S_8 and 4.867Ω for $\text{Fe}_3\text{Co}_3\text{Ni}_3\text{S}_8$, while the faradaic resistance arising from recombination reactions and electrochemical ad-/desorption (R_p) is at 0.749 and 0.625Ω , respectively (Table S7). For $\text{Fe}_{4.5}\text{Ni}_{4.5}\text{S}_8$, the faradaic resistances R_{CT} and R_p are 5.507 and 0.869Ω in sum higher, explaining the comparably lower performance during the HER. Correlating this again to ΔE_H , it becomes evident that just the right binding strength is required for a good performance during the HER. Alongside with the results for the overpotentials, this agrees well with the finding that compounds with a high iron content have a stronger affinity for hydrogen atoms, while nickel has the opposite effect—lowering the reaction rates overall in both cases. The results from the Tafel analysis can also be linked well to the calculations. A Volmer–Heyrovsky-based mechanism was estimated for the examples Co_9S_8 and $\text{Fe}_3\text{Co}_3\text{Ni}_3\text{S}_8$, which favor mainly bridging μ_2 -hydrides on their active sites during catalysis. Here, seemingly the hydride mobility is a little higher for trimetallic compounds where iron is involved in hydride binding, compared to the pure Co-bound hydride in

Co_9S_8 . This could also be reflected in the comparably lower R_p value of the trimetallic compound resulting in better mean performance during the HER. In contrast, for $\text{Fe}_{4.5}\text{Ni}_{4.5}\text{S}_8$, a Volmer–Tafel-type reaction path was described, enabled by the terminal binding of hydrides on the Fe sites, which in turn are even more mobile on the catalysts surface, favoring the surface recombination. However, the gEIS data suggest that this process does not result in faster reaction rates, due to the higher faradaic resistances. The deactivation behavior of Co_9S_8 and also other Co-rich compounds could be attributed to the formation of strongly adsorbed hydrogen species on the surface, probably involving bonding interactions to Co, which hamper the lateral mobility of adsorbed H-species, their recombination on the surface, as well as desorption upon reaction with additional protons, albeit not entirely preventing them. This would be consistent with the calculated results indicating stronger μ_2 -H bonds on Co-containing surfaces, a less pronounced deactivation at higher temperatures as well as the conservation of ECSA. In total, introducing Co as well as other foreign metals to the Pn-lattice noticeably influences the typical Pn-type HER mechanisms and activity. This behavior can be exploited to tune the electrochemical activity. Furthermore, circumventing S-depletion may provide a useful option in the design of metal chalcogenide catalysts for usage under conditions where a partial release of sulfur has to be avoided, not to mention the preservation of the original catalyst composition.

CONCLUSIONS

In summary, we herein demonstrated the preparation of a variety of trimetallic pentlandite compounds $(\text{Fe,Co,Ni})_9\text{S}_8$ based on iron, cobalt, and nickel. Hydrogen adsorption energies were determined by means of DFT calculations and correlated with various HER performance indicators. Along this line, several activity phenomena could thus be described with good accuracy. It was found that an approximately equal distribution of iron and nickel led to an increase in performance peaking at an equimolar ratio of Fe, Co, and Ni. This observation could be well explained by DFT calculations, as the ideal binding strength of hydrogen to CoCo or FeCo centers focused the adsorption energy in a preferred region of about -0.24 eV as described for the well-known HER catalyst platinum. The mechanism was also decisively altered by the corresponding presence or absence of one of the transition metals. While Co_9S_8 exhibited a comparatively high Tafel slope (Volmer step with a rate-

limiting Heyrovsky step) and $\text{Fe}_{4.5}\text{Ni}_{4.5}\text{S}_8$ exhibited a comparatively low Tafel slope (Volmer step followed by Tafel step), the values of the trimetallic compounds, such as $\text{Fe}_3\text{Co}_3\text{Ni}_3\text{S}_8$, were located at a sweet-spot (mainly Volmer–Heyrovsky). From a stability perspective, the phase-pure trimetallic compounds are much more durable than Co_9S_8 , maintaining their activity for a prolonged electrolysis time at -300 mA cm^{-2} . Moreover, the activity of the $(\text{Fe},\text{Co},\text{Ni})_9\text{S}_8$ did not change over the duration of electrolysis due to the absence of any sulfur depletion mechanism, as is the case with the bimetallic FeNi variants, thus preserving the original composition.

■ ASSOCIATED CONTENT

SI Supporting Information

The Supporting Information is available free of charge at <https://pubs.acs.org/doi/10.1021/acsmaterialsau.2c00016>.

Materials, experimental procedures, and characterization parameters (Section S1); materials synthesis (Section S2); differential scanning calorimetry (Section S3); powder X-ray diffraction (Section S4); scanning electron microscopy/energy-dispersive X-ray spectrometry (Section S5); X-ray photoelectron spectroscopy (Section S6); single-crystal X-ray diffraction (Section S7); Tafel analysis (Section S8); linear sweep voltammetry (Section S9); electrochemical surface area (Section S10); chronopotentiometry curves (Section S11); density functional theory calculations (Section S12); electrochemical impedance spectroscopy (Section S13); and galvanostatic measurement in a PEM setup (Section S14) (PDF)

■ AUTHOR INFORMATION

Corresponding Authors

Marek P. Checinski – *Creative Quantum, 12489 Berlin, Germany*; Email: marek.checinski@creative-quantum.eu
Ulf-Peter Apfel – *Ruhr-University Bochum, 44801 Bochum, Germany; Fraunhofer UMSICHT, 46047 Oberhausen, Germany*; orcid.org/0000-0002-1577-2420; Email: ulf.apfel@rub.de

Authors

Mathias Smialkowski – *Ruhr-University Bochum, 44801 Bochum, Germany*
Daniel Siegmund – *Fraunhofer UMSICHT, 46047 Oberhausen, Germany; Ruhr-University Bochum, 44801 Bochum, Germany*
Kenta Stier – *Creative Quantum, 12489 Berlin, Germany*
Lars Hensgen – *Tribotec GmbH, 9601 Arnoldstein, Austria*

Complete contact information is available at: <https://pubs.acs.org/doi/10.1021/acsmaterialsau.2c00016>

Notes

The authors declare no competing financial interest.

■ ACKNOWLEDGMENTS

The authors gratefully acknowledge funding from Tribotec GmbH. U.-P.A. is grateful for the financial support by the Deutsche Forschungsgemeinschaft (under Germany's Excellence Strategy–EXC-2033–Project Number 390677874) and the Fraunhofer Internal Programs under grant no. Attract

097-602175 as well as CINES. The authors are grateful to Stephan Spöllmann (RUBION) for measuring the XPS data, and Julian Kleinhaus, Tobias Kull, Sebastian Sanden, as well as David Tetzlaff for the helpful discussion and sharing of time and resources. The authors also thank Dr. Andrzej Miłkuła (AGH UST Krakow) for the very productive scientific dialog. They especially thank Leonard Messing and Lucas Hoof for their support and provision of the data from the PEM experiments. D.S. gratefully acknowledges funding from the BMBF in the framework NanoMatFutur (“H2Organic”, project number 03XP0421). U.P.A., D.S. and L.H. acknowledge financial support from the BMWK (“CO₂-syn”, project number: 03EE5104A).

■ ABBREVIATIONS

| | |
|------|--------------------------------------|
| CP | chrono potentiometry |
| CV | cyclic voltammetry |
| DFT | density functional theory |
| DSC | differential scanning calorimetry |
| EDX | energy-dispersive X-ray spectrometry |
| HER | hydrogen evolution reaction |
| LSV | linear sweep voltammetry |
| PGM | platinum group metals |
| PXRD | powder X-ray diffraction |
| SEM | scanning electron microscopy |
| XRD | single-crystal X-ray diffraction |

■ REFERENCES

- (1) Siegmund, D.; Metz, S.; Peinecke, V.; Warner, T. E.; Cremers, C.; Grevé, A.; Smolinka, T.; Segets, D.; Apfel, U.-P. Crossing the Valley of Death: From Fundamental to Applied Research in Electrolysis. *JACS Au* **2021**, *1*, 527–535.
- (2) Zhu, J.; Hu, L.; Zhao, P.; Lee, L. Y. S.; Wong, K.-Y. Recent Advances in Electrocatalytic Hydrogen Evolution Using Nanoparticles. *Chem. Rev.* **2020**, *120*, 851–918.
- (3) Konkena, B.; Puring, K.; Sinev, I.; Piontek, S.; Khavryuchenko, O.; Duerholt, J. P.; Schmid, R.; Tueysuez, H.; Muhler, M.; Schuhmann, W.; Apfel, U.-P. Pentlandite Rocks as Sustainable and Stable Efficient Electrocatalysts for Hydrogen Generation. *Nat. Commun.* **2016**, *7*, No. 12269.
- (4) Tetzlaff, D.; Pellumbi, K.; Baier, D. M.; Hoof, L.; Shastry Barkur, H.; Smialkowski, M.; Amin, H. M. A.; Grätz, S.; Siegmund, D.; Borchardt, L.; Apfel, U.-P. Sustainable and Rapid Preparation of Nanosized Fe/Ni-Pentlandite Particles by Mechanochemistry. *Chem. Sci.* **2020**, *11*, 12835–12842.
- (5) Qin, W.; Hu, B.; Bao, D.; Gao, P. The Preparation of Co₉S₈ and CoS₂ Nanoparticles by a High Energy Ball-Milling Method and Their Electrochemical Hydrogen Storage Properties. *Int. J. Hydrogen Energy* **2014**, *39*, 9300–9306.
- (6) Zhang, Y.; Gao, Q.; Wang, S. Hydrothermal Impregnation Synthesis of Cobalt Pentlandite as Anode Material of H₂S SOFC. *Ionics* **2016**, *22*, 743–749.
- (7) Bezverkhyy, I.; Afanasiev, P.; Danot, M. Preparation of Highly Dispersed Pentlandites (M,M')₉S₈ (M, M' = Fe, Co, Ni) and Their Catalytic Properties in Hydrodesulfurization. *J. Phys. Chem. B* **2004**, *108*, 7709–7715.
- (8) Bezverkhyy, I.; Danot, M.; Afanasiev, P. New Low-Temperature Preparations of Some Simple and Mixed Co and Ni Dispersed Sulfides and Their Chemical Behavior in Reducing Atmosphere. *Inorg. Chem.* **2003**, *42*, 1764–1768.
- (9) Sugaki, A.; Kitakaze, A. High Form of Pentlandite and Its Thermal Stability. *Am. Mineral.* **1998**, *83*, 133–140.
- (10) Piontek, S.; Andronescu, C.; Zaichenko, A.; Konkena, B.; junge Puring, K.; Marler, B.; Antoni, H.; Sinev, I.; Muhler, M.; Mollenhauer, D.; Roldan Cuenya, B.; Schuhmann, W.; Apfel, U.-P. Influence of the Fe:Ni Ratio and Reaction Temperature on the Efficiency of (Fe)_x(Ni)_{1-x}

x)9S8 Electrocatalysts Applied in the Hydrogen Evolution Reaction. *ACS Catal.* **2018**, *8*, 987–996.

(11) Smialkowski, M.; Siegmund, D.; Pellumbi, K.; Hensgen, L.; Antoni, H.; Muhler, M.; Apfel, U.-P. Seleno-Analogues of Pentlandites (Fe₄SNi₄SS₈–YSeY, Y = 1–6): Tuning Bulk Fe/Ni Sulphoselenides for Hydrogen Evolution. *Chem. Commun.* **2019**, *55*, 8792–8795.

(12) Smialkowski, M.; Tetzlaff, D.; Hensgen, L.; Siegmund, D.; Apfel, U.-P. Fe/Co and Ni/Co-Pentlandite Type Electrocatalysts for the Hydrogen Evolution Reaction. *Chin. J. Catal.* **2021**, *42*, 1360–1369.

(13) Pellumbi, K.; Smialkowski, M.; Siegmund, D.; Apfel, U.-P. Enhancing the CO₂ Electroreduction of Fe/Ni-Pentlandite Catalysts by S/Se Exchange. *Chem. – Eur. J.* **2020**, *26*, 9938–9944.

(14) Apfel, U.-P.; Hensgen, L.; Smialkowski, M. Use of Sulfidic Compositions. WIPO Patent WO2020169806A12020.

(15) Mikula, A.; Dąbrowa, J.; Kusior, A.; Mars, K.; Lach, R.; Kubowicz, M. Search for Mid- and High-Entropy Transition-Metal Chalcogenides – Investigating the Pentlandite Structure. *Dalton Trans.* **2021**, *50*, 9560–9573.

(16) Kim, Y.; Karuppanan, M.; Lee, D.; Bae, H. E.; Luong, Q. T.; Kang, S. Y.; Sung, Y.-E.; Cho, Y.-H.; Kwon, O. J. (Fe, Ni, Co)₉S₈@CS Catalyst Decorated on N-Doped Carbon as an Efficient Electrocatalyst for Oxygen Evolution Reaction. *Int. J. Energy Res.* **2022**, *46*, 3145–3154.

(17) Junge Puring, K.; Piontek, S.; Smialkowski, M.; Burfeind, J.; Kaluza, S.; Doetsch, C.; Apfel, U.-P. Simple Methods for the Preparation of Non-Noble Metal Bulk-Electrodes for Electrocatalytic Applications. *J. Vis. Exp.* **2017**, *124*, No. e56087.

(18) Knop, O.; Ibrahim, M. A. Chalkogenides of the transition elements: II. Existence of the π phase in the M₉S₈ section of the system Fe–Co–Ni–S. *Can. J. Chem.* **1961**, *39*, 297–317.

(19) Li, H.; Qian, X.; Xu, C.; Huang, S.; Zhu, C.; Jiang, X.; Shao, L.; Hou, L. Hierarchical Porous Co₉S₈/Nitrogen-Doped Carbon@MoS₂ Polyhedrons as PH Universal Electrocatalysts for Highly Efficient Hydrogen Evolution Reaction. *ACS Appl. Mater. Interfaces* **2017**, *9*, 28394–28405.

(20) Li, Y.; Yin, Z.; Cui, M.; Liu, X.; Xiong, J.; Chen, S.; Ma, T. Interface Engineering of Transitional Metal Sulfide–MoS₂ Heterostructure Composites as Effective Electrocatalysts for Water-Splitting. *J. Mater. Chem. A* **2021**, *9*, 2070–2092.

(21) Wu, J.; Wang, X.; Jiang, J.; Lin, W.; Zhu, S.; Sha, J.; Ma, L.; Zhao, N. In-Situ Synthesis of MoS₂/Co₉S₈ Heterostructure for Efficient HER Electrocatalyst. *Mater. Lett.* **2021**, *292*, No. 129621.

(22) Zegkinoglou, I.; Zendegani, A.; Sinev, I.; Kunze, S.; Mistry, H.; Jeon, H. S.; Zhao, J.; Hu, M. Y.; Alp, E. E.; Piontek, S.; Smialkowski, M.; Apfel, U.-P.; Körmann, F.; Neugebauer, J.; Hickel, T.; Roldan Cuenya, B. Operando Phonon Studies of the Protonation Mechanism in Highly Active Hydrogen Evolution Reaction Pentlandite Catalysts. *J. Am. Chem. Soc.* **2017**, *139*, 14360–14363.

(23) Bentley, C. L.; Andronesco, C.; Smialkowski, M.; Kang, M.; Tarnev, T.; Marler, B.; Unwin, P. R.; Apfel, U.-P.; Schuhmann, W. Local Surface Structure and Composition Control the Hydrogen Evolution Reaction on Iron Nickel Sulfides. *Angew. Chem., Int. Ed.* **2018**, *57*, 4093–4097.

(24) Lindqvist, M.; Lindqvist, D.; Westgren, A. The Crystal Structure of Co₉S₈ and of Pentlandite (Ni,Fe)₉S₈. *Sven. Kem. Tidskr.* **1936**, *48*, 156–160.

(25) Prewitt, C. T.; Rajamani, V. Thermal Expansion of the Pentlandite Structure. *Am. Mineral.* **1975**, *60*, 39–48.

(26) Thomas, J. G. N. Kinetics of Electrolytic Hydrogen Evolution and the Adsorption of Hydrogen by Metals. *Trans. Faraday Soc.* **1961**, *57*, 1603–1611.

(27) Voiry, D.; Yamaguchi, H.; Li, J.; Silva, R.; Alves, D. C. B.; Fujita, T.; Chen, M.; Asefa, T.; Shenoy, V. B.; Eda, G.; Chhowalla, M. Enhanced Catalytic Activity in Strained Chemically Exfoliated WS₂ Nanosheets for Hydrogen Evolution. *Nat. Mater.* **2013**, *12*, 850–855.

(28) Eady, S. C.; Peczonczyk, S. L.; Maldonado, S.; Lehnert, N. Facile Heterogenization of a Cobalt Catalyst via Graphene

Adsorption: Robust and Versatile Dihydrogen Production Systems. *Chem. Commun.* **2014**, *50*, 8065–8068.

(29) Li, Y.; Wang, H.; Xie, L.; Liang, Y.; Hong, G.; Dai, H. MoS₂ Nanoparticles Grown on Graphene: An Advanced Catalyst for the Hydrogen Evolution Reaction. *J. Am. Chem. Soc.* **2011**, *133*, 7296–7299.

(30) Sabatier, P. Hydrogénations et déshydrogénations par catalyse. *Ber. Dtsch. Chem. Ges.* **1911**, *44*, 1984–2001.

(31) Zhu, C. R.; Gao, D.; Ding, J.; Chao, D.; Wang, J. TMD-Based Highly Efficient Electrocatalysts Developed by Combined Computational and Experimental Approaches. *Chem. Soc. Rev.* **2018**, *47*, 4332–4356.

(32) Nørskov, J. K.; Bligaard, T.; Logadottir, A.; Kitchin, J. R.; Chen, J. G.; Pandelov, S.; Stimming, U. Trends in the Exchange Current for Hydrogen Evolution. *J. Electrochem. Soc.* **2005**, *152*, J23.

(33) Chen, M.; Smart, T. J.; Wang, S.; Kou, T.; Lin, D.; Ping, Y.; Li, Y. The Coupling of Experiments with Density Functional Theory in the Studies of the Electrochemical Hydrogen Evolution Reaction. *J. Mater. Chem. A* **2020**, *8*, 8783–8812.

(34) Nørskov, J. K.; Abild-Pedersen, F.; Studt, F.; Bligaard, T. Density Functional Theory in Surface Chemistry and Catalysis. *Proc. Natl. Acad. Sci. U.S.A.* **2011**, *108*, 937–943.

(35) Trasatti, S. Work Function, Electronegativity, and Electrochemical Behaviour of Metals. *J. Electroanal. Chem. Interfacial Electrochem.* **1972**, *39*, 163–184.